

Influence of Annealing Temperature on Photocatalytic and Electrochemical Sensing Properties of SnO₂/ZnO Nanocomposites

Atif Mossad Ali^{1,2,*}, Omniat Qreshah³, Adel A. Ismail⁴, Farid A. Harraz^{4,5}, Hamed Algarni¹, Mohd Faisal⁵, Wee Siong Chiu⁶

¹ Department of Physics, Faculty of Science, King Khalid University, Abha, Saudi Arabia

² Department of Physics, Faculty of Science, Assiut University, Assiut, Egypt

³ Physics Department, Faculty of Arts & Science, Najran University, Saudi Arabia

⁴ Nanostructured Materials and Nanotechnology Division, Central Metallurgical Research and Development Institute, Cairo, Egypt

⁵ Promising Centre for Sensors and Electronic Devices (PCSED), Advanced Materials and Nano-Research Centre, Najran University, Najran, Saudi Arabia

⁶ Low Dimensional Materials Research Centre, Department of Physics, Faculty of Science, University of Malaya, Kuala Lumpur, Malaysia

*E-mail: atifali@kku.edu.sa

Received: 20 February 2018 / *Accepted:* 24 March 2018 / *Published:* 5 June 2018

SnO₂/ZnO nanocomposites were prepared by sol-gel technique in the presence of polyethylene glycol, followed by annealing at various temperatures ranging from 600 to 1000 °C. The prepared SnO₂/ZnO were studied by XRD, FTIR, FT-Raman, TEM, UV–vis DR spectroscopy, photoluminescence spectroscopy, and nitrogen adsorption-desorption isotherm analysis. The crystal phases and energy gap of the SnO₂/ZnO nanocomposites were modified with annealing temperatures. The photocatalytic activity of the prepared SnO₂/ZnO nanocomposites for the decomposition of methylene blue (MB) dye was examined under visible light illumination. It was found that photodegradation rate of the prepared photocatalysts for the decomposition of MB decreased linearly upon increasing the annealing temperature from 600 to 1000 °C. The maximum photocatalytic efficiency (100%) was obtained for the SnO₂/ZnO nanocomposite annealed at 600 °C. The photocatalytic activity of the SnO₂/ZnO nanocomposite was dependent on their surface areas and bandgap values. The optimal SnO₂/ZnO nanocomposite annealed at 600 °C was also used for the electrochemical sensing of liquid ethanol showing significant sensing response with a high sensitivity of 20.09 μAmM⁻¹cm⁻² and a limit of detection of 25.2 μM ethanol concentration.

Keywords: SnO₂/ZnO; Nanocomposites; Sol-gel; Photocatalyst; Photodegradation

1. INTRODUCTION

In past few decades, the metal oxide semiconductor nanocomposites have studied as one of the most important research topics due to important applications in the field of environmental purification and solar energy applications [1,2]. Among different semiconductor metal oxides, SnO₂ and ZnO are the most favorable candidates for high-performance sensors and photocatalysts. When SnO₂ and ZnO are merged, the heterojunction nanostructures can greatly enhance their physical properties [2]. Further, electron transportation properties, the composite materials established on zinc and/or tin oxide find interesting use in photovoltaic applications, photo/-catalysis, and in transparent conducting oxides as solar electrodes [3,4].

ZnO is a well-known material with wide E_g of 3.37 eV at room temperature and possess large 60 meV exciton energy. In addition, ZnO has high transmission entire UV-Vis region, and exhibits important properties like low toxicity, photocatalytic efficiency, and good stability in reductive chemical environments [5]. Furthermore, it also exhibit exclusive electro-optical properties for various applications [6, 7] like fuel cells [8], gas sensors [9], and photocatalysts [10] among a host of others. Several studies have reported on different form of ZnO for photodegradation process for water treatment applications [11, 12]. On the other hand, SnO₂ is belonging to tetragonal structure with oxygen deficiency and shows E_g of 3.6 eV. Its high optical transparency and electrical conductivity leads to extremely appealing applications in spintronic devices [13]. On the other hand, SnO₂ is employed in a variety of fields [14] like white pigments for conductive coatings, TCO's for electrodes, surge arrestors [15], catalysts [16], optoconducting coatings for solar cells [17]. Minami et al. [18] in their study reported that SnO₂/ZnO binary oxides could combine the benefits of both ZnO and SnO₂. SnO₂/ZnO composites, in spite of having difficulties in chemical etching particularly at higher concentrations of metallic Sn, may substitute the existing transparent conductive oxides in certain applications. As both Zn and Sn are more abundant than indium, SnO₂/ZnO composites can emerge as the low-cost alternatives. These two materials have the combined advantage of possessing excellent thermal and mechanical strength can be used as electrodes in batteries [19], solar cells [20], sensors [21], transistors [22], and photocatalysts [23]. The combination of these two materials provides high photocatalytic activity than the single material by extending the photoresponsive range and increasing the charge separation rate [24].

The SnO₂ nanoparticles are prepared by different methods like precipitation [25], hydrothermal synthesis [26], sol-gel [27], hydrolytic [28], carbothermal reduction [29], and polymeric precursor method [30]. Similarly, for the preparation of ZnO nanoparticle, many techniques have been used such as PLD [31], CVD [32], MBE [33], magnetron sputtering [34], and sol-gel [35]. The sol-gel method is most common, as it enables the development of low-cost films and provides large surface area and high-quality films for many applications.

In present work, we report synthesis of SnO₂/ZnO nanocomposites by sol-gel technique using polyethylene glycol and annealed at 600- 1000 °C. The photocatalytic activity of these prepared nanocomposites was studied by photodegradation MB dye under visible light irradiation. In addition, the as-synthesized SnO₂/ZnO nanocomposite was employed as a sensing active material for the

electrochemical sensing of ethanol in aqueous solutions with a high sensitivity of $20.09 \mu\text{AmM}^{-1}\text{cm}^{-2}$ and a limit of detection of $25.2 \mu\text{M}$ ethanol concentration.

2. EXPERIMENTAL DETAILS

2.1 Sample Preparation

SnO_2/ZnO nanocomposite was synthesized by the sol-gel technique using polyethylene glycol (PEG). The precursor solution was obtained by mixing PEG, distilled water, and zinc acetate ($\text{Zn}(\text{CH}_3\text{COO})_2 \cdot 2\text{H}_2\text{O}$). The mixed solutions of these were stirred for about 30 min to complete the hydrolysis resulting in the formation of the sol. The desired amount of Tin tetrachloride 5-hydrate ($\text{SnCl}_4 \cdot 5\text{H}_2\text{O}$) was added to ZnO sol and magnetically stirred for 2 h to obtain the 0.1 $\text{SnO}_2/1.0 \text{ ZnO}$ molar ratio. The white suspension was then dried at 120°C for 24 h. Finally, the prepared samples were annealed at different temperatures (600, 800, 900, and 1000°C).

2.2 Characterization

To identify the structural properties of SnO_2/ZnO nanocomposites XRD technique is employed with Cu $K\alpha$ radiation ($\lambda = 1.5406 \text{ \AA}$). FT-Raman spectroscopy employed to record the Raman spectra of SnO_2/ZnO nanocomposites. The vibrational studies were carried out by usual method of pressing nanopowders into KBr pellets and were recorded in the range of 400 to 4000 cm^{-1} . The Diffuse reflectance spectra of the prepared samples were recorded in the range of 200 to 800 nm using a UV/Vis spectrometer. The photoluminescence (PL) spectra of all the samples were determined in the UV to the near-IR region at excitation $\lambda = 230 \text{ nm}$. The nitrogen adsorption-desorption isotherms were obtained using a NOVA2000e (Quantachrome, USA) instrument. A JEM-2100F field emission transmission electron microscope with the highest analytical performance in the 200 kV class with a probe size under 0.5 nm was used.

2.3 Photocatalytic Testing

Photocatalytic experiments of SnO_2/ZnO nanocomposites were conducted by the degradation of methylene blue (MB) as probe molecule under visible light irradiation (250 W visible lamps). In each experiment, before illumination 1 g/L of synthesized SnO_2/ZnO nanocomposite per 100 mL of MB (0.02 mM) as a model pollutant was stirred in the dark for 120 minutes to obtain adsorption equilibrium. The suspension solution was withdrawn at regular intervals and centrifuged to remove the photocatalyst before analysis. The MB ($\lambda_{\text{max}} = 663 \text{ nm}$) was analyzed by measuring a change in the absorbance using UV-visible spectrophotometer (Lambda 950, Perkin Elmer).

2.4 Electrochemical Sensing of Liquid Ethanol

The nanocomposite with optimal composition of 0.1 SnO₂/1.0 ZnO (annealed at 600 °C) was smoothly coated onto glassy carbon electrodes (GCE) (Bio-Logic SAS) after its initial pretreatment using 1 μm and 0.05 μm polishing diamond and alumina slurry respectively. The coating process was conducted via mixing the nanocomposite with a butyl carbitol acetate and ethyl acetate as binders. The as-coated, modified electrodes were dried at 65 °C for 5 h. An electrochemical workstation, ZahnerZennium, Germany was used for the electrochemical measurements using either a two electrode system or a three electrode set-up. The SnO₂/ZnO modified GCE acts as a working electrode, a Pt wire serves as a counter electrode, whereas Ag/AgCl reference electrode is used in case of cyclic voltammetric measurements only.

3. RESULTS AND DISCUSSION

3.1 Morphological, Structural, Optical, and Photocatalytic Properties

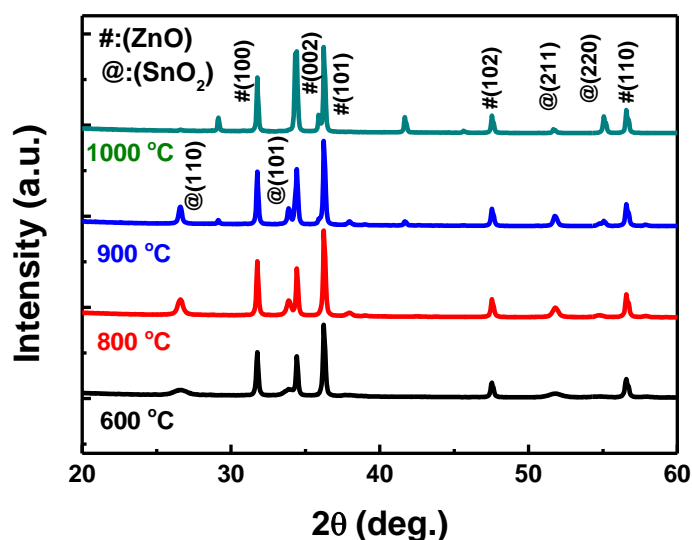


Figure 1. XRD patterns of SnO₂/ZnO nanocomposite annealed at different temperatures.

The XRD spectra of the SnO₂/ZnO nanocomposites are displayed in Fig. 1. Fig. 1 shows hexagonal wurtzite structures polycrystalline nature as established by the diffraction peaks equivalent to (100), (002), and (101) planes at the angles 31.2°, 33.95° and 36.19°, respectively [33]. The intensity of the main diffraction peak (equivalent to (101) plane at ~36.19°) increased with increasing the annealing temperature. The patterns also displayed the representative SnO₂ peaks centered at 2θ = (33.77°, 51.56° and 54.92°) due to (101), (211), and (220) planes, respectively. In other words, the polycrystalline structure of the SnO₂/ZnO nanocomposite was considered to be a mixture of ZnO (wurtzite) and SnO₂ (tetragonal rutile structure). With the increasing annealing temperature, the crystallinity is generally improved, thus an increase in the peak intensity indicated an enhancement in

the crystallinity of the SnO₂/ZnO nanocomposite [36]. The intensity of SnO₂ (220) increased while that of SnO₂ (211) decreased on increasing the annealing temperature, which may have resulted due to the development of SnO₂/ZnO microstructure, caused by excessive annealing temperature. The observation of a strong ZnO (101) peak indicates a highly orientated growth.

To identify the functional groups of all the nanocomposites, the FT-IR spectroscopy was recorded at different annealed temperatures (Fig. 2). A distinct band appear about 542 cm⁻¹ could be attributed to the vibrational modes of Zn-O bonds, and confirmed the formation of the metal oxide nanostructures [37,38]. The intensity of this band decreased with the rising annealing temperatures. The band at 437 cm⁻¹ observed at 600 °C corresponded to ZnO. The position of this band shifted to smaller wavenumbers at high annealing temperatures. Porotnikov et al. [39] observed IR modes of 159, 266, 380, 430, 535, 575 and 650 cm⁻¹ for two forms of zinc-stannate. The modes between 150 and 420 cm⁻¹ were attributed to Zn-O bonds, while the frequency modes at 692 cm⁻¹ were a characteristic of the Sn-O bonds [39]. The FT-IR results obtained by Lutz et al. [40] represented typical lattice vibrations with contributions from all the atoms and bonds of the spinel structure. The decrease in the FT-IR band intensity with the increase of annealing temperatures may be explained by the strong interaction between the lattice phonons and a higher charge carrier concentration [41].

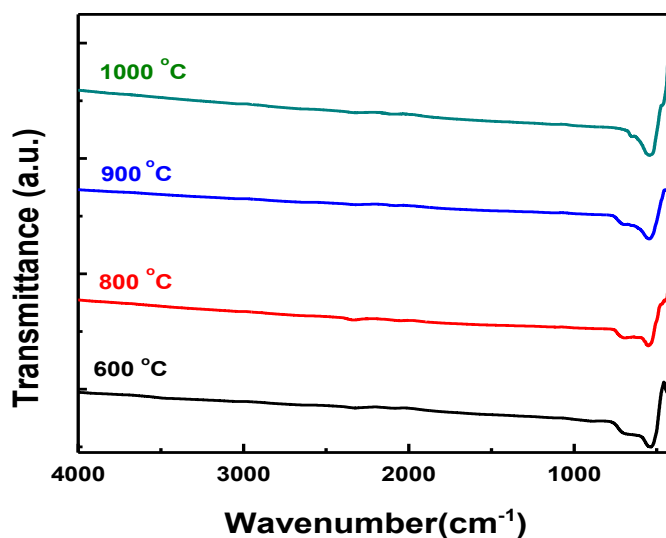


Figure 2. FTIR of SnO₂/ZnO nanocomposite annealed at different temperatures.

Fig. 3 shows the Raman spectra of SnO₂/ZnO nanocomposite measured at different annealing temperatures. The Raman peaks located at 228, 324, 438, 570 and 640 cm⁻¹ corresponded to the optical phonons of SnO₂ and ZnO. The peak at 438 cm⁻¹ was of a nonpolar optical phonon E₂ (high) of wurtzite ZnO and the peaks at 228 and 324 cm⁻¹ were attributed to the second-order Raman spectrum of zone boundary phonons 2-TA(M) and 2-E₂(M), of the hexagonal ZnO [43]. The peak observed at 570 cm⁻¹ was due to the A₁(LO) mode of the hexagonal ZnO. The peak at 640 cm⁻¹ was assigned to the A_{1g} vibrational mode of SnO₂ [44]. It can be seen from Fig. 3 that the intensities of E₂(high) (438 cm⁻¹) and A₁(LO) (570 cm⁻¹) peaks decreased with annealing temperatures whereas that of A_{1g} (640 cm⁻¹) peak increased. The observed peaks confirmed the wurtzite structure for ZnO

nanostructures and tetragonal structure for SnO₂ nanocomposite and provide evidence of both metal oxides within the mixed metal oxide materials with composite nature of the mixtures. The observed results are in good agreement with XRD studies.

To understand the pore structure of SnO₂/ZnO nanocomposite, their N₂ adsorption and desorption isotherms were also measured (Fig. 4). The adsorption amount of N₂ on SnO₂/ZnO annealed at 1000 °C (Fig. 4(d)) was smaller than other samples annealed at 600 °C (Fig. 4 (a)), 800 °C (Fig. 4(b)), and 900 °C (Fig. 9(c)), indicating that SnO₂/ZnO had a lower surface area than other samples. At 600 °C, SnO₂/ZnO had a BET surface area of 11.26 m²/g which was higher than the others. The insets in Fig. 4 correspond to the pore size distribution (PSD) curves were measured by the Barret-Joyner-Halenda (BJH) method. The surface area decreased while the pore size increased with the increasing annealing temperatures.

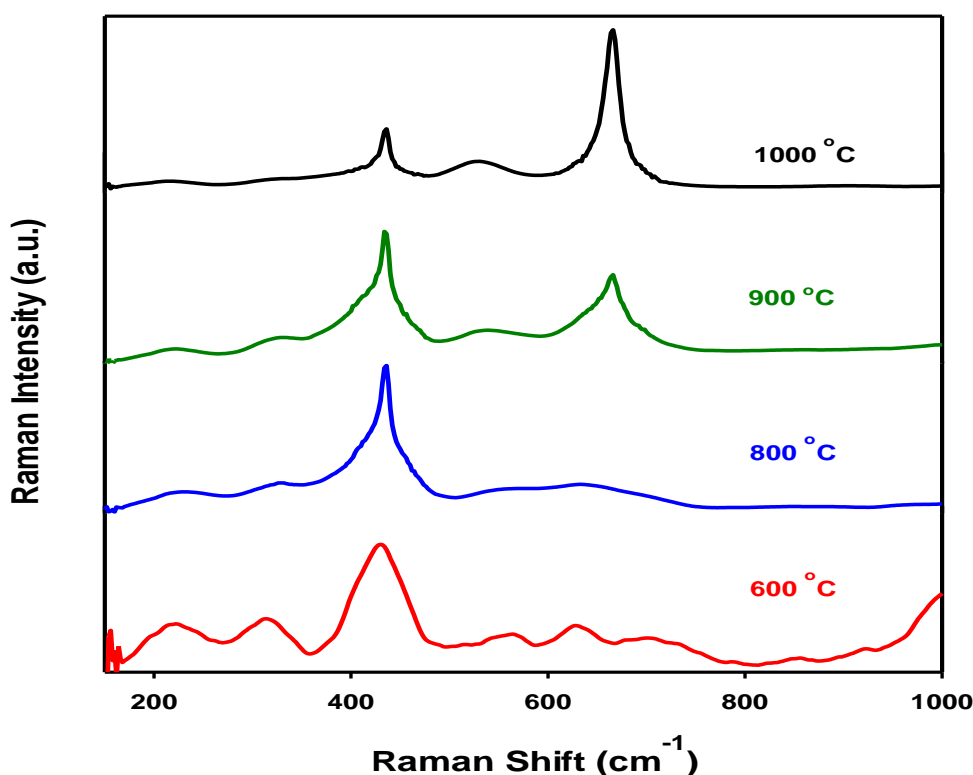


Figure 3. Raman spectroscopy of SnO₂/ZnO nanocomposite annealed at different temperatures.

Fig. 5 shows the typical TEM images of 0.1 SnO₂/1.0 ZnO nanocomposite after annealing at 600 °C, 800 °C, 900 °C and 1000 °C for 4 h. The results exhibited that the prepared nanoparticles and nanorods were formed at 600 °C, Fig. 5(a). The diameter of the prepared nanorods was around 10 nm and length was 100 nm whereas the nanoparticle size was around 10 nm. In addition, a change in the annealing temperature led to a dramatic modification in the diameter (which observed a boost, Fig. 5(b) and Fig. 5(c)) and length of the rods. The prepared nanoparticles were seen to be irregular (Fig. 5(b) & Fig. 5(c)). At high annealing temperature (1000 °C), the results showed that the nanoparticles were agglomerated to large particle sizes. The inset of Fig. 5(c) and Fig. 5(d) show the selected area

electron diffraction (SAED) patterns for the 0.1 SnO₂/1.0 ZnO crystalline structures. The EDX analysis confirms the even intensity of the Sn and Zn signs all over the particles, showing the homogeneous distribution of both the components within the inorganic framework (Fig. 5e). Also, the final content of the atomic percentage of Zn, Sn, and O in the prepared 0.1 SnO₂/1.0 ZnO nanocomposite confirmed that Zn and Sn were determined and the final content was consistent with the starting precursors of the ZnO and SnO₂.

Fig. 6 depicts a diffuse reflectance (DR) micrograph of the SnO₂/ZnO nanocomposite. The reflectance spectra at 600, 800, 900 and 1000 °C showed similar shapes. In addition, from figure 6 it is understood that with increasing the annealing temperature absorption edge is shifts from the UV to the near visible region which is important in solar efficiency. The Kubelka-Munk (K-M) function F(R) against reflectivity R is plotted using the following relation $F(R) = (1-R)^2/2R$. The band gap (E_g) of the SnO₂/ZnO material was calculated from [45-49];

$$F(R)=A(h\nu-E_g)^n/h\nu \tag{1}$$

where *A*, *hν* and *n* have their usual meanings and the value of *n* depends on the probability of transition it is equal to 2 for a direct band gap or 1/2 for an indirect band gap. The E_g can be calculated from the tangent lines of the [F(R) E]² Vs photon energy as shown in Fig. 7.

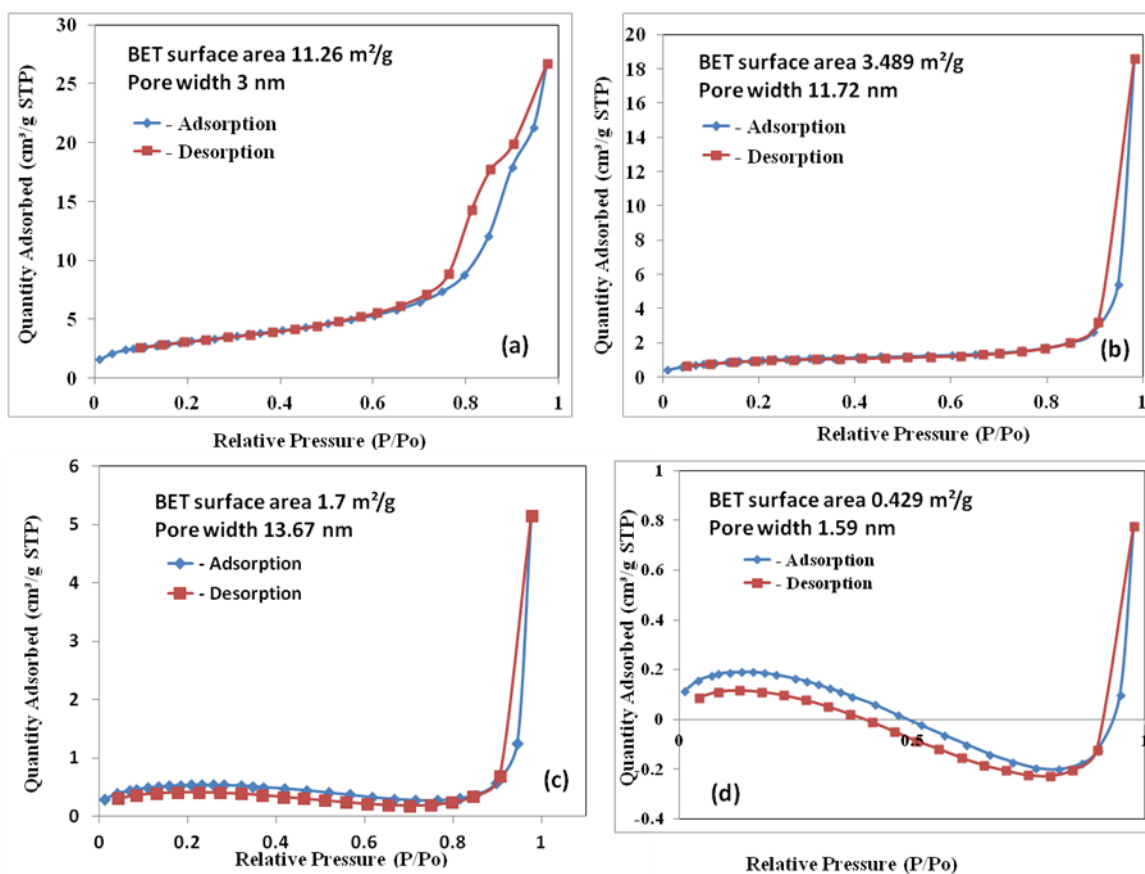


Figure 4. N₂ adsorption isotherms of SnO₂/ZnO nanocomposite annealed at 600 °C (a) 800 °C (b) 900 °C (c) and 1000 °C (d).

Generally, an increase in the annealing temperature indications to a rise in the mean grain size and a decrease in the energy gap (E_g) [50]. It is concluded that in case of particle size is small in semiconductors it is not evident. Sheng et al. [51] reported that when calcination of ZnO particles at 500 to 700 °C, the mean grain size increased from 60.3 nm to 215 nm and the E_g is increased from 3.17 eV to 3.19 eV [51]. In the present work, the E_g of SnO₂/ZnO nanocomposite was found to be 2.98, 3.01, 3.02, and 3.01 eV at annealing temperature 600 °C, 800 °C, 900 °C and 1000 °C (Fig. 7(a, b, c, d)), respectively. These values were very less compare to both the pure oxides SnO₂ and ZnO. This relative variation in the E_g after increasing the annealing temperature could be explained by the variation of the particle size in the nanoregime.

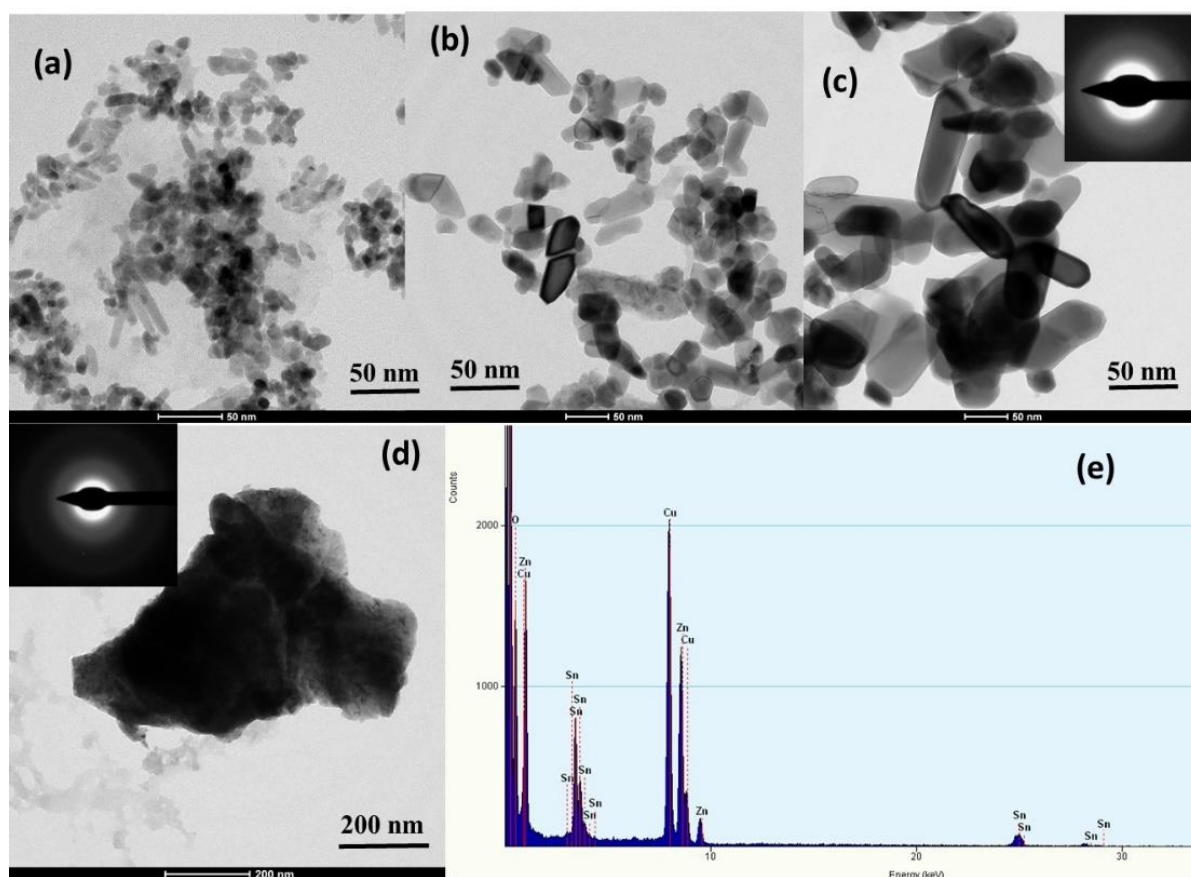


Figure 5. TEM images of 0.1 SnO₂/1.0 ZnO nanocomposite after annealing at 600 °C (a), 800 °C (b), 900 °C (c) and 1000 °C (d) for 4 h. The insets in (c) and (d) show the SAED patterns for the 0.1 SnO₂/1.0 ZnO crystalline structures, Energy dispersive X-ray spectra (EDX) of 0.1 SnO₂/1.0 ZnO nanocomposite after annealing at 600 °C (e).

The photocatalytic reaction was done under visible light in the absence of the photocatalyst to estimate the methylene blue (MB) degradation. It was found that there was no loss in the content of MB in the absence of the photocatalyst after 2 h which indicated that it was not easy to degrade methylene blue under visible light illumination. This degradation of methylene blue was followed by absorption spectra measurement at regular intervals by a UV/vis spectrophotometer. Fig. 8 displays the variation in absorption spectra of methylene blue in the existence of (SnO₂/ZnO) for different annealing temperatures under visible light at different time intervals.

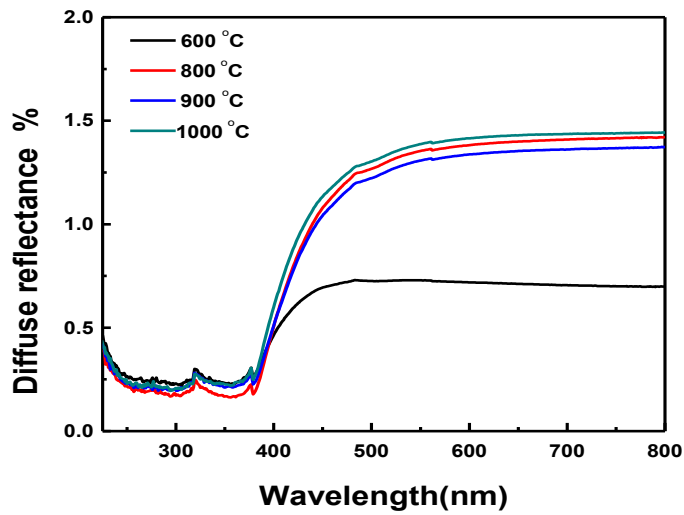


Figure 6. UV-visible spectra of SnO₂/ZnO nanocomposite annealed at different temperatures.

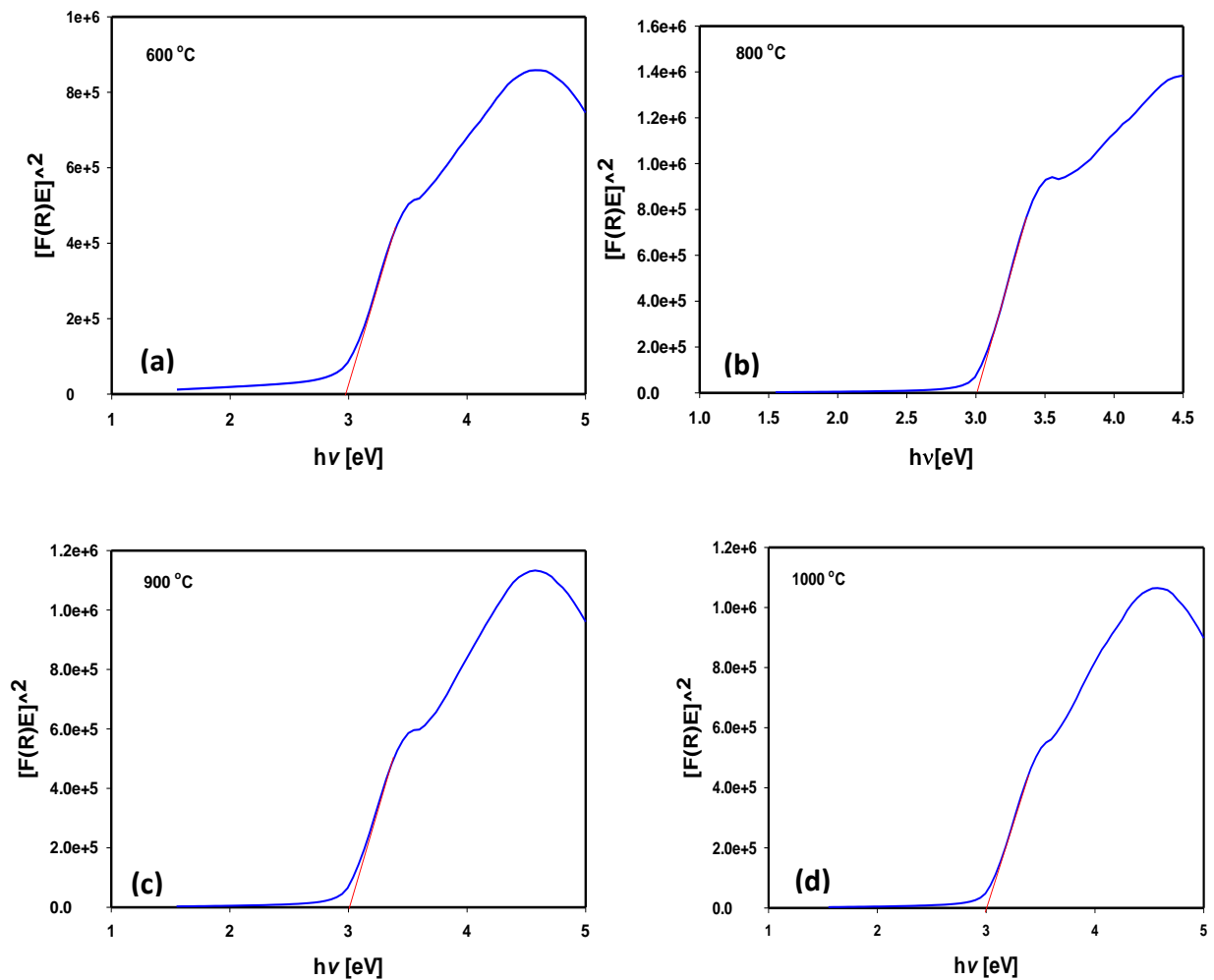


Figure 7. The plot of transferred Kubelka-Munk versus energy of the light absorbed of the SnO₂/ZnO nanocomposite annealed at different temperatures.

For all the temperatures, a strong absorption band located at $\lambda=245$ nm, $\lambda=291$ nm, and $\lambda=663$ nm was observed for a gradual decrease in the MB dyes with increasing irradiation times that completely vanished after 120 min. The absorption band located at $\lambda=245$ nm disappeared after 60 min. methylene blue can be decolorized into colorless form i.e., leuco-MB, either by the oxidative degradation of the dye or by the two-electron reduction.

The absence of an absorption band at $\lambda=245$ nm of leuco-MB clearly indicated that a decoloration of methylene blue can be mainly attributed to the oxidative degradation of the dye in the presence of photocatalyst. The absorbance of $\lambda=663$ nm (i) at 600 °C: was observed to decrease from 1.40 to 0.03 (Fig. 8(a)), (ii) at 800 °C: from 1.34 to 0.58 (Fig. 8(b)), (iii) at 900 °C: from 1.34 to 0.06 (Fig. 8(c)) and (iv) at 1000 °C: from 1.26 to 0.1 (Fig. 8(d)), all after (about) 2 h of illumination.

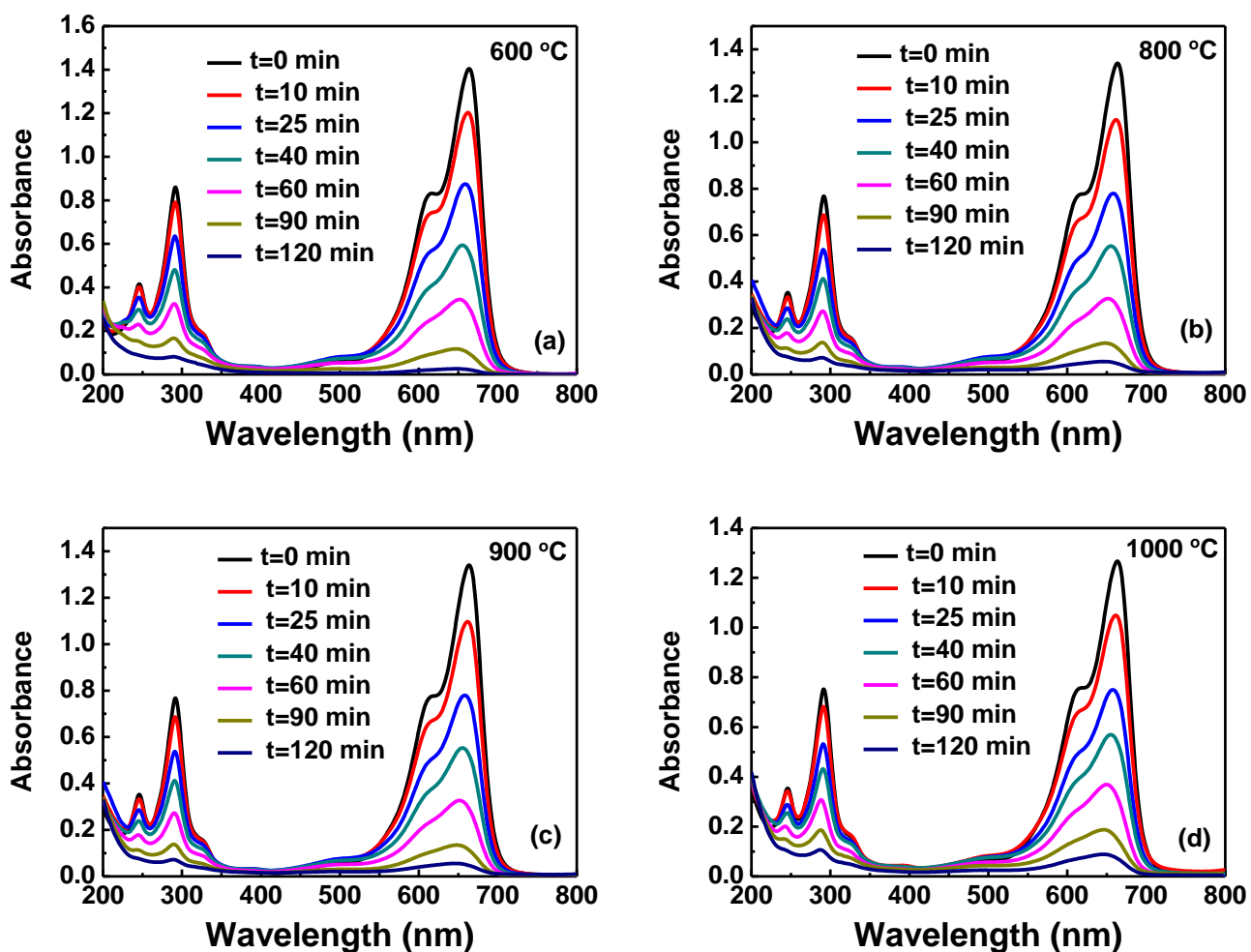


Figure 8. Absorbance vs. wavelength as a function of illumination time for the photocatalytic degradation of methylene blue (MB) on SnO₂/ZnO nanocomposite annealed at different temperatures.

Fig 9 shows the relationship between C/C_0 and irradiation time for SnO₂/ZnO nanocomposite annealed at different temperatures. From this figure the degradation rate of MB was decreased with the increase of annealing temperature of SnO₂/ZnO nanocomposite. The photocatalytic activity was

significantly reduced at higher annealing temperature as a result of the variation in phase composition and particle size. Wang et al. [53] reported that SnO₂/ZnO nanocomposite annealed at low temperature consisted of only of ZnO and SnO₂ with no observation of the Zn₂SnO₄ phase. In addition, Zn₂SnO₄ emerged only at high annealing temperatures and comparatively exhibited a poor photocatalytic activity [53]. Moreover, higher annealing temperature caused the growth of particles, an observation supported by XRD, leading to a decrease in the surface areas resulting in a decrease in the photocatalytic activity [54,55].

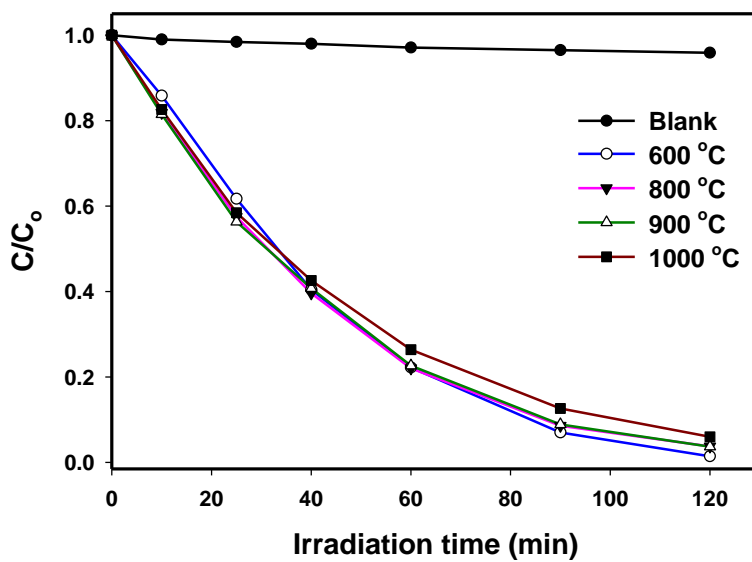


Figure 9. Concentration vs. irradiation time for SnO₂/ZnO nanocomposites with different annealing temperatures.

The photodegradation rate of MB was found to decrease with the increase of annealing temperatures (Fig. 10). This phenomena is explained due to growing size of the particles leading to a low surface area and increase in crystallinity with temperature. As shown at the sample annealed at 600 °C, it is shown the highest specific surface area (11.26 m²/g) with less crystalline than others annealed at 1000 °C with the lowest specific surface area (0.429 m²/g) is in good agreement with TEM results (Fig. 5). The specific surface area plays a key role in the photocatalytic degradation of the dye molecules. On the basis of the photocatalytic mechanism [56], the highly reactive OH[•] and O₂^{•-} are produced on the surface of sample under visible light illumination. Therefore, the surface characteristics of nanocomposites will greatly influence their photocatalytic activity. On the basis of above analysis, the SnO₂/ZnO catalyst showed the best photocatalytic activity due to its superior morphology and better crystallinity. The second reason for improving the photocatalytic performance a transfer of charge carriers from a semiconductor to another is possible, leading to a more efficient electron-hole separation and a higher photocatalytic activity. Since both ZnO and SnO₂ are n-type semiconductors, it is possible to locate their valence band edge by adding the band gap energy to the flat-band potential value. The corresponding results indicated that the valence and conduction bands of

ZnO ($E_{VB} = 2.84$ eV, $E_{CB} = -0.36$ eV) were lower than that of SnO₂ ($E_{VB} = 3.44$ eV, $E_{CB} = -0.11$ eV) [52].

Photoluminescence (PL) spectrometer is an important instrument to understand the most charge carrier trapping, migration, and transfer, i.e., to explain photo generated e⁻/h⁺ pairs in particular material created recombination of the mentioned photo generated pairs [56]. PL spectra of the SnO₂/ZnO nanocomposite at the excitation $\lambda=325$ nm (3.83 eV) is shown in Fig. 11.

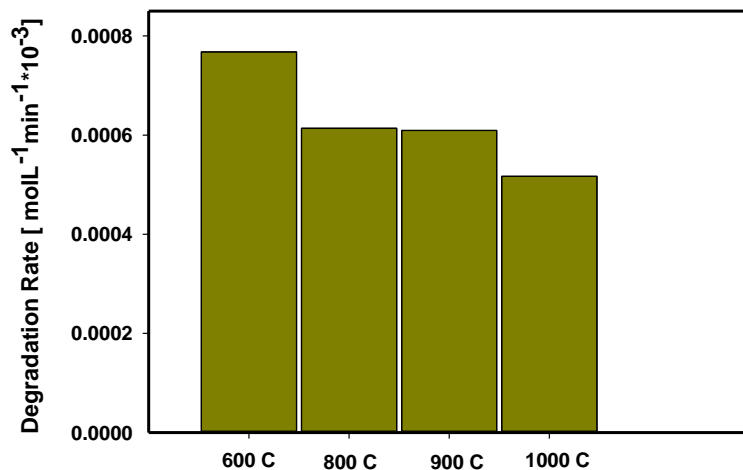


Figure 10. Degradation rate of the SnO₂/ZnO nanocomposites with MB at different annealing temperatures.

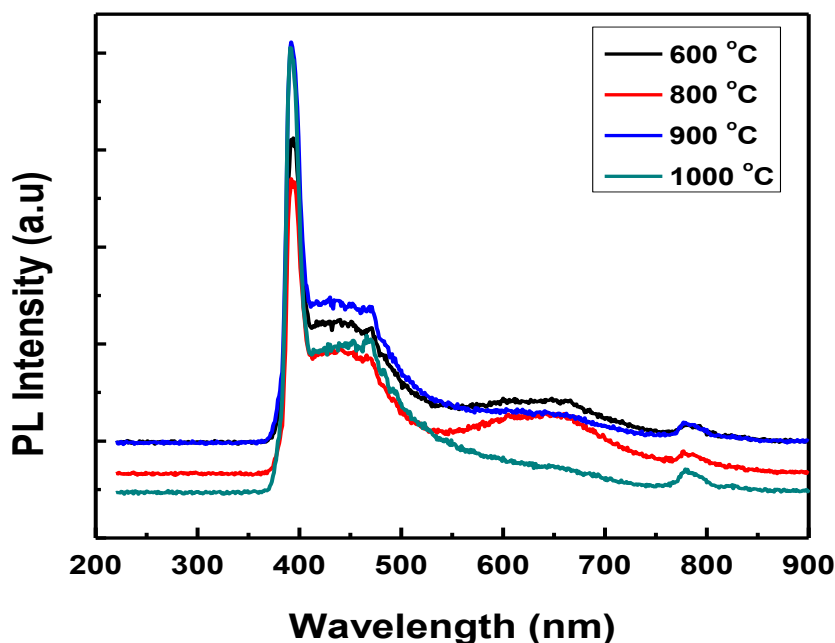


Figure 11. Photoluminescence (PL) of SnO₂/ZnO nanocomposite annealed at different temperatures.

A high emission band was observed at 391 nm (3.17 eV) and 468 nm (2.65 eV). The two unknown broad peaks located at 659 nm (1.88 eV) and 780 nm (1.59 eV) nm were also observed. PL mechanism of SnO₂ is still unclear and hard to be observed [52]. The direct gap transitions are produced due to oxygen vacancy defects and provide possible PL [57].

In the SnO₂/ZnO structure all the SnO₂ molecules are surrounded by ZnO. When this structure is exposed to excitation wavelength, the excitation wavelength was almost absorbed by ZnO and as a result, the PL peaks from the SnO₂ could not emerge out. Li et al. [58] reported that SnO₂ nanostructures can break the dipole-forbidden rule and realize UV luminescence, from the SnO₂ nanowires [57]. Here, the UV emission band observed at 391 nm was attributed to the band edge recombination of the photo-generated carriers due to conduction band to acceptors and neutral-donor-bound excitons. Moreover, the mechanism of the blue emission at 468 nm was unclearly established. Xu and Wang [59] reported a green, blue and near UV emissions at 437-455 nm, a band at 455 nm were attributed to a neutral oxygen vacancy [60] and the green emission of 468 nm, related to the intrinsic defect structures. The potential difference between ZnO and SnO₂ allows photoelectrons to easily migrate from the ZnO surface to the SnO₂ conduction band. This result leads to a decrease in the radiation combination of photoinduced electrons on the ZnO surfaces. In addition, the intensity of the emission bands increased as the annealing temperatures increased owing to the thermal generation of regional defects in the sample [60].

3.2 Electrochemical Sensing of Liquid Ethanol at Modified glassy carbon electrodes (GCE)

As a first step, the electrochemical behavior of modified glassy carbon electrodes (GCE) working electrodes was examined by cyclic voltammetry (CV) technique. The electrochemical measurements were conducted in a redox couple composed of 5 mmol/L potassium hexacyanoferrate [Fe(CN)₆]^{3-/4-} and 50 mmol/L KCl solution at a scan rate of 100 mV/s at room temperature and stagnant condition. Fig. 12 shows the CVs obtained at bare GCE, pure ZnO modified GCE and SnO₂/ZnO modified GCE. A pair of small redox peaks was detected in case of using bare GCE with 8.4 μA anodic current at 530 mV (black curve). Such a smallest redox peaks indicates sluggish electron transfer at the bare GCE interface. For pure ZnO modified GCE (blue curve), an increased redox peaks was observed with 12.2 μA anodic current with a lower potential shift to 500 mV. Further enhancement in redox peaks was obtained in case of using SnO₂/ZnO nanocomposite modified GCE (red curve), in which a current increment to 16.8 μA with a relatively potential shift to the value 490 mV was detected. This result indicates a significant enhancement of the electrocatalytic activity of modified electrodes compared to bare electrode. Additionally, the peak current measured at the nanocomposite modified electrode was much larger than other electrodes, which suggests a faster electron transfer related reactions and hence would allow an efficient sensing behavior to liquid ethanol at the SnO₂/ZnO modified GCE.

The SnO₂/ZnO nanocomposite modified GCE was then used for sensing ethanol in aqueous solution by applying a simple current-potential (*I-V*) approach. The as-recorded *I-V* characteristics in 0.1M PBS of pH 7 at a scan rate of 50 mVs⁻¹ in various ethanol concentrations (0.05 to 16 mM) are collectively shown in Fig. 13(a). As could be revealed, the recorded current response increased as the

ethanol concentration increased in solution. The enhanced current response is likely attributed to an increase in solution ionic strength. The calibration curve showing the relation between ethanol concentration and average current values of the above I - V data is plotted in Fig. 13(b). As could be noted, two different slope values for two different linear regions were obtained. The initial linear region corresponds to the lower ethanol concentration from 0.05 to 1.0 mM and the second one is related to the higher concentration range from 1.0 to 16 mM ethanol. Fitting of the linear equations (2) and (3) was done for both concentration regions as follows:

$$\text{Lower ethanol concentration (R}^2=0.9589\text{): } I (\mu\text{A}) = 1.4263 [\text{ethanol}] (\mu\text{A}) + 0.2262 \quad (2)$$

$$\text{Higher ethanol concentration (R}^2=0.9941\text{): } I (\mu\text{A}) = 0.08497 [\text{ethanol}] (\mu\text{A}) + 1.4828 \quad (3)$$

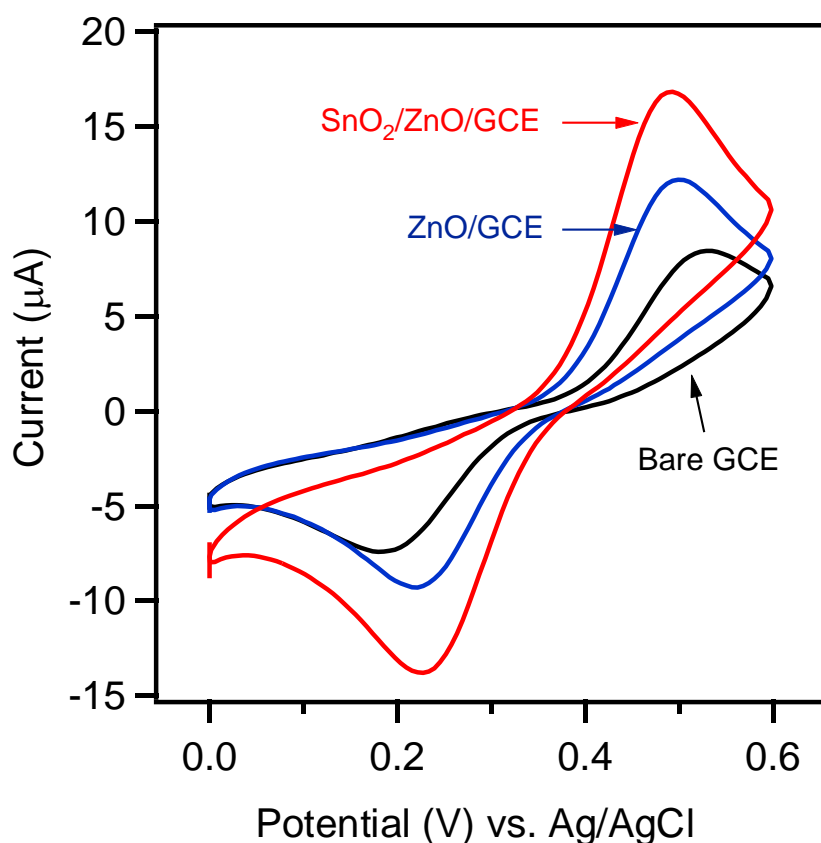


Figure 12. Cyclic voltammograms of bare GCE, pure ZnO modified GCE and 0.1 SnO₂/1.0 ZnO modified GCE, in 5 mmol/L potassium hexacyanoferrate (1:1) [Fe(CN)₆]^{3-/4-} and 50 mmol/L KCl solution at a scan rate 100 mV/s.

The electrode sensitivity was accordingly calculated as the ratio (slope of calibration plot/electrode surface area: 0.071 cm²); the sensitivity values were estimated as 20.09 μAmM⁻¹cm⁻² at lower concentration region and 1.20 μAmM⁻¹cm⁻² at higher concentration regime. The significant decrease in sensitivity at higher ethanol concentration is probably attributed to the electrode surface saturation with ethanol. Such different sensitivity regions have been observed earlier during ethanol sensing at different modified electrodes [61,62]. The reason behind such different sensitivity regions was suggested to be related to different modes of ethanol adsorption onto the modified surface

electrode. At lower concentration region, the ethanol adsorption proceeds via a physisorption mode, whereas a chemisorption process dominates at higher concentration region [61]. As an important sensing parameter, the limit of detection (LOD) of the current electrode sensor was estimated based on signal-to-noise ratio ($S/N=3$) and according to the following equation [63]:

$$\text{LOD} = 3 S_b/m \quad (4)$$

where (S_b) is the standard deviation value measured in a blank sample for five current measurements and was found to be $0.012 \mu\text{A}$, and m represents the slope at lower concentration region ($1.42630 \mu\text{AmM}^{-1}$). The LOD value was then calculated as $25.2 \mu\text{M}$.

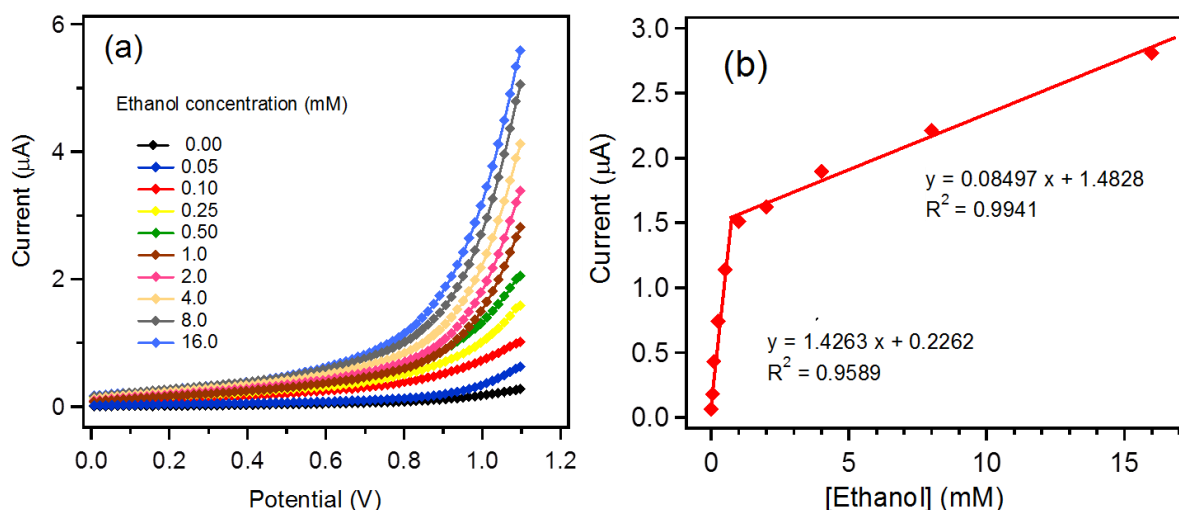


Figure 13. (a) Current-potential (I - V) characteristics as a function of various ethanol concentrations ranging from 0.05 to 16 mM, measured using 0.1 $\text{SnO}_2/1.0 \text{ ZnO}$ modified GCE in PBS of pH 7. (b) The corresponding calibration plot.

4. CONCLUSION

In present study, the SnO_2/ZnO nanomaterial was prepared by sol-gel method. The influence of annealing temperatures on the structural and optical properties of SnO_2/ZnO nanocomposite was studied. The E_g of SnO_2/ZnO was found to be 2.98, 3.01, 3.02, and 3.01 eV after annealing at 600, 800, 900 and 1000 °C, respectively. The PL spectrum of the SnO_2/ZnO nanocomposite was recorded at the excitation $\lambda = 325 \text{ nm}$ (3.83 eV), a high emission peak was observed at 391 nm (3.17 eV) with a broad emission band detected at 780 nm (1.59 eV). The photocatalytic activity of SnO_2/ZnO nanocomposite reached the maximum at 600°C. The order of photocatalytic performance at temperatures: 600 °C > 800 °C > 900 °C > 1000 °C may be due to a low surface area and increase in the crystallinity with temperature. With the optimal SnO_2/ZnO nanocomposite, liquid ethanol was electrochemically detected over the concentration range 0.05-16 mM, giving a high sensitivity $20.09 \mu\text{AmM}^{-1}\text{cm}^{-2}$ and lower detection limit $25.2 \mu\text{M}$.

ACKNOWLEDGEMENTS

The authors extend their appreciation to the Deanship of Scientific Research at King Khalid University for funding this work through research groups program under grant number R.G.P. 1/20/38

References

1. J. Sundaramuthy, N. Li, P.S. Kumar, S. Ramakrishna, *Biofuel. Res. J.*, 2 (2014) 44.
2. Z.Q. Liu, L.X. Ding, Z.L. Wang, Y.C. Mao, S.L. Xie, Y.M. Zhang, G.R. Li, Y.X. Tong, *Crys. Eng. Comm.*, 14 (2012) 2289.
3. H. Zeng, G. Duan, Y. Li, S. Yang, X. Xu, W. Cai, *Adv. Funct. Mater.*, 20 (2010) 561.
4. T. Minami, *Semicond. Sci. Technol.*, 20 (2005) 35.
5. Y.X. Wang, X.Y. Li, G. Lu, X. Quan, G.H. Chen, *J. Phys. Chem. C*, 112 (2008) 7332.
6. M.H. Huang, S. Mao, H. Feick, H.Q. Yan, Y.Y. Wu, H. Kind, E. Weber, R. Russo, P.D. Yang, *Sci.*, 292 (2001) 1897.
7. Z.L. Wang, J.H. Song, *Science*, 312 (2006) 242.
8. O. Kluth, G. Schöpe, J. Hüpkes, C. Agashe, J. Müller, B. Rech, *Thin Solid Films*, 442 (2003) 80.
9. P. Mitra, A.P. Chatterjee, H.S. Maiti, *J. Mater. Sci.*, 9 (1998) 441.
10. C.H. Ye, Y. Bando, G.Z. Shen, D.J. Golberg, *Phys. Chem. B*, 110 (2006) 15146.
11. Q. Wan, T.H. Wang, J.C. Zhao, *Appl. Phys. Lett.*, 87 (2005) 083105.
12. F.M. Meng, X.P. Song, Z.Q. Sun, *Vacuum*, 83 (2009) 1147.
13. S. khafory, N. Talib, M.H. Suhail, *Appl. Phys.*, 8 (2016) 10.
14. D.S. Ginley, C. Bright, *MRS Bull.*, 25 (2000) 15.
15. S.A. Pianaro, P.R. Bueno, E. Longo, J.A. Varela, *J. Mater. Sci. Lett.*, 14 (1995) 692.
16. P.W. Park, H.H. Kung, D.W. Kim, M.C. Kung, *J. Catal.*, 184 (1999) 440.
17. K.L. Chopra, S. Major, D.K. Pandya, *Thin Solid Films*, 102 (1983) 1.
18. T. Minami, H. Sonohara, S. Takata, H. Sato, *Jpn. J. Appl. Phys.*, 33 (1994) 1693.
19. F. Belliard, J. T. S. Irvine, *J. Power Sources*, 97–98 (2001) 219.
20. S. Ito, Y. Makari, T. Wada, S. Yanagida, *J. Mater. Chem.*, 14 (2004) 385.
21. S.P. Yawale, S.S. Yawale, G.T. Lamdhade, *Sens. Actuators. A*, 135 (2007) 388.
22. M.G. McDowell, R.J. Sanderson, I.G. Hill, *Appl. Phys. Lett.*, 92 (2008) 013502.
23. W.W. Wang, Y.J. Zhu, L.X. Yang, *Adv. Funct. Mater.*, 17 (2007) 59.
24. J. Yang, D. Li, X. Yang, L.D. Lu, *J. Solid State Chem.*, 165 (2002) 193.
25. N. Sergent, P. Gelin, L. Perier-Camby, H. Praliaud, G. Thomas, *Sens. Actuators B: Chem.*, 84 (2002) 176.
26. N.S. Baik, G. Sakai, N. Miura, N. Yamazoe, *J. Am. Ceram. Soc.*, 83 (2000) 2983.
27. L. Broussous, C.V. Santilli, S.H. Pulcinelli, A.F. Craievich, *J. Phys. Chem. B*, 106 (2002) 2855.
28. Z.X. Deng, C. Wang, Y.D. Li, *J. Am. Ceram. Soc.*, 85 (2002) 2837.
29. E.R. Leite, J.W. Gomes, M.M. Oliveira, E.J.H. Lee, E. Longo, J.A. Varela, C.A. Paskocimas, T.M. Boschi, F. Lanciotti, P.S. Pizani, P.C. Soares, *J. Nanosci. Nanotechnol.*, 2 (2002) 125.
30. E.R. Leite, A.P. Maciel, I.T. Weber, P.N. Lisboa, E. Longo, C.O. PaivaSantos, A.V.C. Andrade, C.A. Pakoscimas, Y. Maniette, W.H. Schreiner, *Adv. Mater.*, 14 (2002) 905.
31. X.M. Fan, J.S. Lian, Z.X. Guo, H.J. Lu, *Appl. Surf. Sci.*, 239 (2005) 176.
32. M.R. Waugh, G. Hyett, I.P. Parkin, *Chem. Vap. Deposition*, 14 (2008) 366.
33. Y.F. Chen, N.T. Tuan, Y. Segawa, H.J. Ko, S.K. Hong, T. Yao, *Appl. Phys. Lett.*, 78 (2001) 1469.
34. Q.P. Wang, D.H. Zhang, H.L. Ma, X.H. Zhang, X.J. Zhang, *Appl. Surf. Sci.*, 220 (2003) 12.
35. B. Pal, M. Sharon, *Mater. Chem. Phys.*, 76 (2002) 82.
36. S.M. Lee, Y.H. Joo, C. Kim, *Appl. Surf. Sci.*, 320 (2014) 494.
37. L. Kumaresan, A. Parbhu, M. Palanichamy, E. Arumugam, V. Murugesan, *J. Hazard. Mater.*, 186 (2011) 1183.

38. G.N. Dar, A. Umar, S.A. Zaidi, A.A. Ibrahim, M. Abaker, S. Baskoutas, M. S. Al-Assiri, *Sensors Actuators B* 173 (2012) 72.
39. N.V. Porotnikov, V.G. Savenko, O.V. Sidorova, *J. Inorg. Chem.*, 28 (1983) 983.
40. H.D. Lutz, B. Mueller, H.J. Steiner, *J. Solid State Chem.*, 90 (1991) 54.
41. H. Kuzmany, in: Bernhard Schrader (Ed.). *Infrared and Raman Spectroscopy*, (1995).
42. C.A. Arguello, D.L. Rousseau, S.P.S. Porto, *Phys. Rev.*, 181 (1969) 1351.
43. K.A. Alim, V.A. Fonoberov, M. Shamsa, A.A. Balandin, *J. Appl. Phys.*, 97 (2005) 124313.
44. A. Dieguez, A. Romano-Rodriguez, A. Vila, *J. Appl. Phys.*, 90 (2001) 1550.
45. A.S. Ahmed, M.M. Shafeeq, M.L. Singla, S. Tabassum, A.H. Naqvi, A. Azam, *Journal of Luminescence*, 131 (2010) 1.
46. P. Kubelka, F. Munk, *Z. Tech. Phys.*, 12 (1931) 593.
47. J. Tauc, R. Grigorovici, A. Vanuc, *Phys. Status Solidi*, 15 (1966) 627.
48. A.E. Morales, E.S. Mora, U. Pal, *Rev. Mex. Fis.*, 53 (2007) 18.
49. E. Yassitepe, Z. Khalifa, G.H. Jaffari, C.S. Chou, S. Zulfiqar, M.I. Sarwar, S.I. Shah, *Powder Technol.*, 201 (2010) 27.
50. S. Yang, Y. Liu, Y. Zhang, D. MO, *Bulletin of Materials Science*, 33 (2010) 209.
51. C. Wang, X. Wang, B. Xu, J. Zhao, B. Mai, P. Peng, G. Sheng, J. Fu, *J. Photochem. Photobiol. A*, 168 (2004) 47.
52. A. Hamrouni, N. Moussa, F. Parrino, A. Di Paola, A. Houas, L. Palmisano, *J. Mol. Catal. A: Chem.*, 390 (2014) 133.
53. C. Wang, X.M. Wang, J.C. Zhao, B.X. Mai, G.Y. Sheng, P.A. Peng, J.M. Fu, *J. Mater. Sci.*, 37 (2002) 2989.
54. A. Towata, Y. Uwamino, M. Sando, K. Iseda, H. Taoda, *NanoStruct. Mater.*, 10 (1998) 1033.
55. L.G. Devi, G.M. Krishnaiah, *J. Photochem. Photobiol. A: Chem.*, 121 (1999) 141.
56. X. Wang, H. Fan, P. Ren, *Colloid. Surf. A*, 402 (2012) 53.
57. C.W. Cheng, B. Liu, H. Y. Yang, W. W. Zhou, L. Sun, R. Chen, S. F. Yu, J. X. Zhang, H. Gong, H. D. Sun, H. J. Fan, *ACS Nano*, 3 (2009) 3069.
58. Y.F. Li, W.J. Yin, R. Deng, J. Chen, Q.Y. Yan, B. Yao, H.D. Sun, S.H. Wei, T. Wu, *Asia. Mater.*, 4 (2012) 1.
59. Z.M. Xu, Y.X. Wang, *J. Alloys Compd.*, 555 (2013) 268.
60. A.M. Ali, A.A. Ismail, R. Najmy, A. Al-Hajry, *J. Photochem. Photobiol. A: Chem.*, 275 (2014) 37.
61. A.P. Alivisatos, *Science*, 271(1996) 933.
62. A.A. Ismail, F.A. Harraz, M. Faisal, A.M. El-Toni, A. Al, Hajry, M.S. Al-Assiri, *Superlattices and Microstructures*, 95 (2016)128.
63. G.L. Long, G.D. Winefordner, *Anal. Chem.*, 55 (1983) 712A.

© 2018 The Authors. Published by ESG (www.electrochemsci.org). This article is an open access article distributed under the terms and conditions of the Creative Commons Attribution license (<http://creativecommons.org/licenses/by/4.0/>).